Title

Improving quantitative analysis of spark-induced breakdown spectroscopy: Multivariate calibration of metal particles using machine learning

Authors

Li, Hanyang

Mazzei, Leonardo

Wallis, Christopher D

et al.

Publication Date

2022

DOI

10.1016/j.jaerosci.2021.105874

Peer reviewed

HHS Public Access

Author manuscript

J Aerosol Sci. Author manuscript; available in PMC 2024 April 22.

Published in final edited form as:

J Aerosol Sci. 2022 January ; 159: . doi:10.1016/j.jaerosci.2021.105874.

Improving quantitative analysis of spark-induced breakdown spectroscopy: Multivariate calibration of metal particles using machine learning

Hanyang Li[a,*], **Leonardo Mazzei**[b], **Christopher D. Wallis**[a], **Anthony S. Wexler**[a,b,c,d]

[a]Air Quality Research Center, University of California Davis, Davis, CA, 95616, USA

[b]Mechanical and Aerospace Engineering, University of California, Davis, CA, 95616, USA

[c]Civil and Environmental Engineering, University of California, Davis, CA, 95616, USA

[d]Land, Air and Water Resources, University of California, Davis, CA, 95616, USA

Abstract

We have recently developed a low-cost spark-induced breakdown spectroscopy (SIBS) instrument for *in-situ* analysis of toxic metal aerosol particles that we call TARTA (toxic-metal aerosol real time analyzer). In this work, we applied machine learning methods to improve the quantitative analysis of elemental mass concentrations measured by this instrument. Specifically, we applied least absolute shrinkage and selection operator (LASSO), partial least squares (PLS) regression, principal component regression (PCR), and support vector regression (SVR) to develop multivariate calibration models for 13 metals (e.g., Cr, Cu, Mn, Fe, Zn, Co, Al, K, Be, Hg, Cd, Pb, and Ni), some of which are included on the US EPA hazardous air pollutants (HAPS) list. The calibration performance, adjusted coefficient of determination (R^2) and normalized root mean square error (RMSE), and limit of detection (LOD) of the proposed models were compared to those of univariate calibration models for each analyte. Our results suggest that machine learning models tend to have better prediction accuracy and lower LODs than conventional univariate calibration, of which the LASSO approach performs the best with $R^2 > 0.8$ and LODs of 40–170 ng m^{-3} at a sampling time of 30 min and a flow rate of 15 l min^{-1}. We then assessed the applicability of the LASSO model for quantifying elemental concentrations in mixtures of these metals, serving as independent validation datasets. Ultimately, the LASSO model developed in this work is a very promising machine learning approach for quantifying mass concentration of metals in aerosol particles using TARTA.

*Corresponding author. hynli@ucdavis.edu (H. Li).

Declaration of competing interest

The authors declare that they have no known competing financial interests or personal relationships that could have appeared to influence the work reported in this paper.

Appendix A. Supplementary data

Supplementary data to this article can be found online at https://doi.org/10.1016/j.jaerosci.2021.105874.

Keywords

Machine learning; Multivariate calibration; Spark induced breakdown spectroscopy; Toxic metal particles

1. Introduction

Spark-induced breakdown spectroscopy (SIBS), originally proposed in 1993, is a type of optical emission spectroscopy that uses a high-voltage pulse (i.e., spark) as the excitation source to form a plasma between two rod electrodes (Hunter, Davis, Piper, Holtzclaw, & Fraser, 2000; Hunter, Wainner, Piper, & Davis, 2003). The sample materials in the plasma emit radiation in a broad range of wavelengths, which can be captured by a spectrometer for elemental identification and quantification (Hahn & Omenetto, 2010; Miziolek, Palleschi, & Schechter, 2006). In the past two decades, there has been a growing interest in the use of SIBS for particulate matter monitoring (Diwakar & Kulkarni, 2012; Hunter, Morency, Senior, Davis, & Fraser, 2000; Jung, Yang, & Yoh, 2020; Yang, Jung, Ryu, & Yoh, 2020; Zheng & Kulkarni, 2017; Zheng et al., 2017). Recently, we developed a cost-effective SIBS instrument for near real-time analysis of toxic metal aerosols, which we call the toxic-metal aerosol real time analyzer (TARTA) (Davari & Wexler, 2020; Li, Mazzei, Wallis, Davari, & Wexler, 2021). The collect and analyze scheme of our instrument is identical to that used in Diwakar and Kulkarni (2012), but differs in that TARTA utilizes a nozzle to impact particles onto the electrode rather than a focused electrostatic deposition and less expensive components. We successfully used the instrument to detect multiple toxic metals and calculated the limit of detection (LOD) in the range of 50 ng m^{-3} to 810 ng m^{-3} using univariate calibration methods on tests with particles containing Cr, Cu, Mn, Co, Zn, Fe, and Ni. However, what remains uncertain is whether we can constrain matrix effects and improve detection accuracy during field deployment of the TARTA. Furthermore, improved spectral analysis techniques may lower LODs for the tested metals, which will be beneficial for detecting pollutants at low concentrations and/or improving temporal resolution.

Matrix effects are a concern for laser-induced breakdown spectroscopy (LIBS) and SIBS (Lepore et al., 2017; Takahashi & Thornton, 2017). Spectral interference, a common matrix effect, occurs when the radiation of other components interferes with those of interest (Hahn & Omenetto, 2012). By using a SIBS instrument to analyze unburned carbon in fly ash, Yao, Zhang, Xu, Yu, and Lu (2017) reported that the strong emission line due to the material of electrodes (W at 247.78 nm) hid the relatively weak emission line of C at 247.86 nm. However, it is possible to reduce spectral interference by careful peak selection and better calibration models. Physical matrix effects have also been studied, which can be due to laser (or spark) formation dynamics, instability of plasma position, and variation of measurement conditions (Evans, Pisonero, Smith, & Taylor, 2020; Tognoni & Cristoforetti, 2016). Chemical matrix effects occur if the emission behavior of one element is altered by the presence of other elements in the sample (IUPAC, 2019). Both physical and chemical matrix effects may result in variations in spectral intensities even if the concentration of the analyte is the same in different samples. Therefore, these effects need to be carefully evaluated and compensated during calibration to ensure robustness.

Multivariate calibration tools can account for matrix effects and provide quantification of elemental concentration in spectroscopic analysis (Næs & Martens, 1984; Takahashi & Thornton, 2017). Different from univariate calibration, which relates chemical quantity to one independent variable (e.g., intensity of a strong emission line of the analyte), multivariate calibration quantifies using spectral emissions at multiple wavelengths (Braga et al., 2010; Zaytsev, Krylov, Popov, Zorov, & Labutin, 2018). Multivariate calibration avoids subjective selection of representative wavelengths for the analytes. Instead, the coefficients of the independent variables (in this case, emission lines of analyte) derived by a calibration model determine the relative importance of each peak when calculating the analyte quantity.

Alongside the advances in machine learning methodology and increases in computational capability, analytical chemists have applied different multivariate models to calibrate elemental concentration. For example, partial least squares (PLS) regression is probably the most widely used technique due to its ease of implementation and its ability to handle the situation where the number of samples is less than the number of variables (H. Fu, Jia, Wang, Ni, & Dong, 2018; Wold, Sjöström, & Eriksson, 2001). By assuming a linear relationship between spectrum and elemental quantity, PLS transforms the original spectrum to a group of orthogonal components and builds a calibration model. Other linear approaches, such as least absolute shrinkage and selection operator (LASSO) and principal component regression (PCR), are also good candidates to handle spectral data that may contain collinearities (Bricklemyer, Brown, Turk, & Clegg, 2013; Wang et al., 2018; Yaroshchyk, Death, & Spencer, 2012). To address the potential issue of non-linearity, support vector regression (SVR) and artificial neural network (ANN) have been recently investigated in near-infrared (NIR) spectroscopic analysis (Shao, Bian, Liu, Zhang, & Cai, 2010).

In this work, we investigate the use of SIBS combined with various machine learning approaches to determine the concentration of metal aerosols nebulized from aqueous solutions. Specifically, we tested 13 metals that are of public health significance, including Al, Be, Cd, Co, Cr, Cu, Fe, Pb, K, Mn, Ni, Hg, and Zn. Both linear approaches (LASSO, PCR, and PLS) and a non-linear approach (SVR) have been studied and compared to the behavior of univariate calibration models for each analyte. We also propose a metric of “adjusted LOD” to inter-compare LODs calculated by the models with different numbers of independent variables. The objective of this work is to propose a more robust approach to improve the quantitative analysis of metal particles using TARTA.

2. Methods

2.1. Instrument and particle sampling

The major components of TARTA include a boost converter to provide high voltage, two tungsten (W) electrodes (anode: a needle with a 50 μm tip diameter; cathode: a rod with a diameter of 1 mm) to form an arc gap of 1.5 mm, a capacitor to periodically charge and discharge, a spectrometer to record the emissions, and electronics (e.g., relay, Arduino microcontroller, and optical coupler) to control the system operation. Details of the SIBS system can be found in Davari and Wexler (2020) and Li et al. (2021). Briefly, the capacitor was first charged to 6000 V in 5 s. Then, the capacitor created a high-voltage

arc between the electrodes, which was detected by a photodiode, followed by spectral analysis by a spectrometer (USB 2000, Ocean Optics Inc.). In order to suppress the initial continuum radiation and obtain spectra with clean elemental emission lines, a delay generator introduces a delay of 1.88 μs before spectrum acquisition.

Our study began with development of calibration models for individual metals. Specifically, we investigated metals not only proposed in US EPA Hazardous Air Pollutants (HAPs) list (including Be, Cd, Co, Cr, Pb, Mn, Ni, and Hg, EPA (2017)), but also those of public health concern or used for source apportionment of particulate matter (including Cu, Fe, Zn, Al, and K). Table S1 summarizes the chemical composition and density of different metals. For each element, standard aqueous solutions of metal nitrate salts at different concentrations (1–10 μg ml^{-1}) were prepared. As shown in Fig. 1, aerosols were generated using a nebulizer (MiniHEART, Westmed, Inc.) at a pressure of 125 kPa and a flow rate of 8 l min^{-1}. The particles were then dried by a diffusion dryer and passed to the spark generation enclosure (0.55 m (L) × 0.5 m (W) × 0.42 m (H)) by a vacuum pump (15 l min^{-1} air flow). The enclosure was connected to building exhaust and operated at a small negative pressure to confine toxic particles. In the enclosure, a 1-mm diameter nozzle directed the particles to deposit on the tip of a 1 mm diameter W cathode. After sampling for a predetermined duration, deposition was terminated and sparks were created to obtain spectral data. To obtain sufficient training data and ensure training accuracy, we varied sampling duration from 1 to 20 min for each element and repeated each experimental condition at least three times. Furthermore, multiple sparks ($N > 5$) were performed after each sampling period to clean off the mass loading on the cathode and avoid carryover of particles to subsequent experiments. In addition to SIBS analysis, we used an Aerodynamic Particle Sizer (APS model 3321, TSI Inc.) to determine particle size distribution and mass concentration. The APS measurements show that both individual metals and metal mixtures have a single mode with a geometric mean diameter of 0.55–0.65 μm (Figure S1). When calculating aerosol mass concentration, we extrapolated the raw APS results by taking into consideration the particle mass beyond the lower detection boundary (0.5 μm). In our previous work (Li et al., 2021), we found that the mass concentration calculated from the elemental solutions tended to be greater than the raw APS results for the experiments using <2 μg ml^{-1} solution concentration, because the nebulized small particles were not detected by the APS. Thus, the ratio of the two mass concentrations was used in the present work to correct the APS measurements for different aqueous solutions.

After model development, we performed an independent validation by using the models to determine elemental concentrations of metal mixtures. Three types of mixtures were designed: (1) A mixture consists of 10 of the 13 tested metals (excluding Al, K, and Be, which are randomly selected as control group), with a concentration of 1 μg ml^{-1} for each element; (2) the same mixture of metals, but a concentration of 5 μg ml^{-1} each; and (3) a mixture contains 5 μg ml^{-1} Fe, Zn, K, and Al (abundant in the atmosphere), 1 μg ml^{-1} Mn, Ni, Cu, Pb, Cr, and Hg (less abundant), and 0.5 μg ml^{-1} Co, Cd, and Be (least abundant). More detailed description of the validation datasets can be found in Section 3.4.

2.2. Data preprocessing

2.2.1. Baseline correction and normalization—In order to eliminate the influence of baseline drift on the accuracy of the proposed models, we applied an automatic baseline correction algorithm following Schulze, Foist, Okuda, Ivanov, and Turner (2012). This algorithm iteratively performs zero-order Savitzky–Golay filter and removal of peaks, until the area of peaks stripped from the spectrum reaches a local minimum. During iteration, the size of the filter window is gradually increased to facilitate convergence. The derived baseline is then subtracted from the original spectra to generate the corrected spectrum.

Similar to previous works (Diwakar & Kulkarni, 2012; Li et al., 2021), we summed the spectral response of 5 consecutive sparks after each particle loading to capture the entire signal of the analyte. As seen in Figure S2, the spectral intensity of the fifth spark from each experiment has reduced to the original values before particle loading (i.e., blank, tungsten only), confirming that no residuals are left on the electrode. Therefore, the corrected spectra for each experiment can be expressed as

$$\textit{Corrected spectrum} = \sum_{i=1}^{5} (\textit{Spectrum}_i - \textit{Baseline}_i) \tag{1}$$

However, signal fluctuations remain in the corrected spectra because the same experimental conditions still resulted in different spectral intensities (Figure S3). As this happens to the whole optical range, we suspect that the observed differences are due to physical matrix effects, such as the variation of spark discharge energy and plasma–particle interaction processes. To mitigate signal fluctuations, previous studies have normalize the raw spectrum by the intensity of internal standards (e.g., (Koelmel et al., 2019; Nicolini, 2020; Takahashi & Thornton, 2017),). During SIBS analysis, the emission lines of W electrodes can be treated as internal standards, because any variation that affects the analyte signal will also affect the W signals to the same degree. We therefore normalized the corrected spectra in Eq. (1) by the strongest emission line of W observed over the whole optical range (401.02 nm), namely

$$\textit{Normalized spectrum} = \frac{\textit{Corrected spectrum}}{\textit{Corrected spectral peak}@401.02\textit{nm}} \tag{2}$$

2.2.2. Identification of spectral peaks—Although multivariate calibration techniques can utilize the full spectral range (200–900 nm, n = 2047) to develop models, it is computationally-intensive and time consuming. Furthermore, by comparing calibration models using full spectra and models using signature wavelengths, previous studies found that the latter model has better predictability and accuracy (X. Fu et al., 2017; Khan, Munir, Yu, & Young, 2020; Zheng, Kulkarni, & Dionysiou, 2018). This is because some spectral regions contain noise and useless information, which propagate uncertainties to the estimated quantity. Therefore, we discarded the spectral range with low signal-to-

noise ratios (i.e., beyond 300–800 nm) and used spectral signals at only representative wavelengths. We defined the representative wavelengths to be those where the spectra exhibit sharp peaks. These sharp peaks are due to elements excited in the plasma (e.g., the materials of the electrodes (W and impurities), the tested aerosol metals, and impurities in the aqueous nebulizing solution).

Specifically, we used a peak detection algorithm to automatically identify peaks in the normalized spectra (Yoder, 2021). The algorithm computes the first derivative of the spectra and locates the peaks when the sign of the derivative changes from positive to negative. The algorithm also uses a threshold of minimal peak intensity to exclude the peaks due to spectral noise and low detection efficiency of the spectrometer. An advantage of this algorithm is that it does not require the knowledge of sample composition and corresponding elemental emission lines, so it can effectively detect all spectral peaks without subjectivity.

We next classify the detected peaks of each metal into three categories: (1) Peaks with intensities that remain roughly constant over different experiments. These peaks are due to the elements independent of the composition and concentration of tested samples, such as W, N, and O excited in the plasma. (2) Peaks with intensities proportional to the solution concentration, but belonged to the impurities in the solution. These peaks include Na at 589.4 nm and Ca at 393.1, 396.5, and 422.3 nm (3) The other peaks that do not belong to the former two categories. Only peaks in the last category are expected to vary with analyte concentration so should play a role in multivariate calibration models. We therefore excluded the peaks in the first category by calculating the standard deviation (std) of peak intensities and teasing out the peaks with std <10%. We next excluded the peaks due to the emissions of Na and Ca present in the second category.

We did not manually locate peaks of the tested metals based on the National Institute of Standards and Technology (NIST) atomic spectral database (Ralchenko et al., 2006), because not all emission lines can be easily detected by our spectrometer. To reduce subjectivity and ambiguity when using a subset of emission lines to represent the tested metals, the method presented in this section provides a novel perspective for selecting emission lines for use in multivariate calibration models.

In the last step of data preprocessing, we included the six wavelengths surrounding each peak, three before and three after, and the corresponding intensities to create input datasets for each metal (similar to Zheng et al. (2018)), spanning a ~2 nm wavelength range. Due to the high resolution of the spectrometer (0.35 ± 0.05 nm), a strong element peak typically spans a few data points. Wavelength shifting caused by different experimental settings is expected to be captured by this preprocessing step (Wang et al., 2018).

2.3. Model development

After preprocessing, the final spectra used as input to machine learning models can be written as X_{ij}, where X represents the normalized spectra in Eq. (2), i represents the ith experiment of the investigated metal, and j represents the jth wavelength identified by the method presented in Section 2.2.2. Accordingly, the dependent variable C_{tot} (i) is the integration of mass concentration over the sampling period for the ith experiment:

$$C_{tot}(i) = C_{APS}(i) \times \text{sampling duration}(i) \quad (3)$$

where C_{APS} is the mass concentration derived by the APS (μg m^{-3}), and sampling duration is in minute.

In this work, we applied different machine learning approaches (including LASSO, PLS, PCR, and SVM) to find the optimal calibration model (using the programming language R version 3.6.1). The theory and structure of these approaches have been extensively discussed in the literature (e.g., (Brereton, 2000; Bro, 2003; Li & May 2020; Olivieri, 2018),), so in this section we will restrict our focus to their application to these datasets. Besides machine learning methods which use multiple emission lines for calibration, univariate calibration was also performed for each element for comparison. A list of wavelengths used for univariate analysis can be found in Table 1.

LASSO, a shrinkage method of linear regression, does variable selection based on a penalty term added to the sum of squared residual errors (SSE). As the value of penalty term increases, the model shrinks the coefficients of less relevant independent variables towards zero (Tibshirani, 1996). During model development, the penalty term is tuned until the model achieves an acceptable fit. In this work, we used 3-fold cross-validation and the criterion of “1SE” to determine the best model, where “1SE” is defined as the smallest set of wavelengths that results in mean squared error (MSE) within one standard error of the minimum MSE (Melkumova & Shatskikh, 2017).

To some extent, both PCR and PLS are related to principal component analysis (PCA). PCA finds a small number of principal components (PCs) to capture the greatest amount of variance in the input matrix (I. T. Jolliffe, 1986). PCR then uses these components as input instead of the original spectra to develop a linear regression (Ian T. Jolliffe, 1982). In contrast, PLS utilizes both input and output data to construct a lower dimensional space defined by a number of latent variables (similar to PCs used in PCA), and performs a regression in the new space (Geladi & Kowalski, 1986; Haaland & Thomas, 1988). When developing the models, the optimal numbers of PC and latent variable were determined by leave-one-out cross validation seeking the smallest MSE.

In addition to the linear approaches described above, we have also explored a non-linear approach Support Vector Regression (SVR). SVR was developed based on the principle of support vector machine (SVM), an algorithm used for pattern recognition and classification problems (Cortes & Vapnik, 1995). In SVR, kernel functions (e.g., linear, polynomial, radial) are used to map the original spectra to a high-dimensional space, where regression can be performed (Drucker, Burges, Kaufman, Smola, & Vapnik, 1997). Here we used a radial kernel function with 10-fold cross validation to grid-search hyper-parameters for each element.

2.4. Limit of detection

According to International Union of Pure and Applied Chemistry (IUPAC) recommendations, the following expression defines LOD for univariate calibration:

$$LOD = 3.33\sigma/S \tag{4}$$

where S is the slope of the calibration curve and σ is an estimate of noise in the data, derived using a number of spectra in the absence of metal particles (Allegrini & Olivieri, 2014; Ismail, Imam, Elhassan, Youniss, & Harith, 2004). LOD has the same unit as the dependent variable (C_{tot}, μg m^{-3} × min). To derive LOD in terms of the delivered mass of the tested metals (LOD_{del}, ng), we can simply multiply the LOD in Eq. (4) by carrier gas flow rate (l min^{-1}).

When dealing with LOD of multivariate calibration models, the “S” term in Eq. (4) can be estimated as the inverse vector of the regression coefficients (1/||b||), where || || is the Euclidean norm of a vector (Braga et al., 2010; Zheng et al., 2018). Since SVR is nonlinear, its analysis does not yield an “S”, so we exclude it from the inter-comparison of LODs in Section 3.3.

When comparing LODs, a critical question that needs to be addressed is how to effectively compare models with different numbers of independent variables. We found that the ||b|| term tends to increase with the number of independent variables used in the calibration model. As a result, PCR and PLS models, which use all input wavelengths, tend to have a greater LOD than LASSO and univariate calibration. Similarly, Davari and Wexler (2020) found that the multivariate calibration models based on LASSO have greater LOD than univariate calibration. To fairly compare LODs across different calibration models, we propose a metric “adjusted LOD”:

$$adjusted\ LOD = \frac{n-k-1}{n-1}^{0.5} \times LOD \tag{5}$$

where n is total number of observation and k is the number of independent variables used in the model. This metric is analogous to adjusted coefficient of determination (adjusted R^2), a special form of R^2, which penalizes the addition of independent variables to the model (Yin & Fan, 2001).

3. Results and discussion

3.1. Wavelength selection

We use the normalized spectra derived from the Co experiments as an example to illustrate the peak identification as described in section 2.2 (Fig. 2). The peak detection algorithm successfully detects all sharp peaks, but not shoulders located on sides of the main peaks (e.g., 352.7, 398, and 411.5 nm). We did not include shoulder peaks in the following

analysis, as they appear not to be related to most of the tested elements — with one exception (Cd) explained below. The sharp peaks were then grouped into three categories as described in Section 2.2.2 (marked by different colors), based on the similarity of intensities across different experiments and prior knowledge of the emission lines of impurities (Na and Ca). After excluding the peaks attributed to categories 1 and 2, three peaks remain at 340.9, 345.1, and 350.4 nm. Lastly, seven independent variables of each peak (one central peak, and three additional wavelengths on each side) are used as input data to develop machine learning models of Co.

In the first three columns of Table 1, we summarized the number of peaks generated by the peak detection algorithm and the final number of central peaks used for each element in model development. One may notice that Cd has 15 final peaks, which is two times more than the other metals. This is because Cd exhibits a peak at 508.7 nm, which is on the shoulder of the sharp peak at 506.9 nm (Figure S4). To account for this shoulder peak, we have to lower the noise threshold used in the peak detection algorithm. As a result, the algorithm yields more peaks, hence yielding more explanatory variables in the Cd model.

Table 1 also shows a list of elemental emission lines obtained from the NIST database. To develop univariate models, we used the strongest emission line of each element within the wavelength range 300–800 nm and free from W interference. We also compared the peak wavelengths obtained at the preprocessing stage (e.g., the three peaks at the wavelengths around 345 nm in Fig. 2) to these theoretical analytical lines and found that the two results correspond well to each other, confirming the reasonability of data preprocessing (Table S1).

The main advantage of using the LASSO approach is that it can both select important variables and estimate regression coefficients. After obtaining the models, variable importance of projection (VIP) was used for qualitative evaluation of the selected independent variables as described in Chong and Jun (2005). As seen in Table 1, the LASSO approach selected one to four wavelengths for the tested metals. Compared to the NIST reference emission lines, the selected wavelengths typically include a strong elemental emission line and a few wavelengths around it. Our results demonstrate that although multiple distinct peaks have been input to the model, one elemental peak seems to be sufficient for the LASSO approach to estimate the analyte concentration. However, when applying LASSO to the Cr data, the model selects only one independent variable (426.1 nm) which does not belong to any analyte peaks. Interestingly, we noticed that Cr has two adjacent strong emission lines at 425.4 and 427.2 nm, which forms a local valley at 426.1 nm (Figure S5). As a result, spectral intensities at both peak and valley wavelengths change with Cr concentrations. Because the goal of LASSO is to build a model with a smaller number of independent variables, it appears to select the valley wavelength to better capture spectral variances from ~424 to 428 nm.

In contrast to LASSO which does feature selection, the other three approaches (PCR, PLS, and SVM) use all preprocessed wavelengths to construct calibration models. Based on VIP scores obtained from the models, we ranked all regression coefficients by their contributions to the prediction and listed the top three important wavelengths in Table 1. Except for Cd and Hg, the important wavelengths for the other metals correspond to one, or several,

strong emission line(s). For example, PCR detects Cr peaks at ~520, 442, and 357 nm as the top influential wavelengths. Similarly, PLS and SVR select wavelengths around two peaks of Cr as the most important contributors. These results are very different from those obtained by LASSO, which is mainly due to their different model fitting concepts. During our preliminary examination of Cd and Hg spectra, we could not easily detect their peaks for the experiments with relatively low solution concentrations and short sampling durations. As a result, it is not surprising that PCR, PLS, and SVR fail to capture the true analyte peaks during model development.

Consequently, the framework of our machine learning models appears to be very competitive with univariate calibration models to provide elemental quantification. In particular, our framework does not rely on prior knowledge of spectral signals from the NIST database, but instead, the model results provide insight into spectral lines related to the sample and differentiated from background due to solution impurities and the tungsten electrodes.

3.2. Performance evaluation using statistical metrics

In this section, the performance of the developed models is evaluated using adjusted R^2 and normalized root mean squared error (normalized RMSE = $\sqrt{MSE}/\bar{Y}$, where $\bar{Y}$ is the mean of dependent variable). In general, high R^2 and low RMSE values indicate a good fit of the model for the training dataset. For most of the elements shown in Fig. 3, the calibration models yield similar adjusted R^2 and normalized RMSE. Despite that, the performance of SVR is noticeably worse than the other machine learning models. This implies that complicated non-linear approaches are not necessarily needed for calibration if we have well constrained matrix effects during preprocessing. Compared to univariate calibration models, LASSO, PCR, and PLS have obtained a slight improvement in accuracy for Al, Be, Co, Cr, Cu, Fe, Ni, and Pb. When comparing across the various elements, the model performance is quite similar, with the best fit for Cu (adjusted $R^2 \approx 0.97$, normalized RMSE ≈ 0.02) and the worst fit for Cd (adjusted $R^2 \approx 0.80$, normalized RMSE ≈ 0.13).

3.3. LOD estimation and comparison with other analytical methods

Detection limit of the TARTA can be expressed in terms of either the LOD of the mass delivered in the air sampling system, LOD_{del} (ng), or the LOD of that atmospheric aerosol mass concentration (LOD_{conc}, μg m^{-3}). The relationship between the two LODs is given in Eq. (6).

$$LOD_{conc} = \frac{LOD_{del}}{\text{sampling time} \times \text{flow rate}} \quad (6)$$

where sampling time is in minute and flow rate is in l min^{-1}. The product of sampling time and flow rate is also known as sampling volume. Ideally, very low LOD_{conc} can be achieved if adequate sampling volume is available, however this requires either a big pump or a loss of temporal resolution. Thus, to satisfy common monitoring needs, we assume a flow rate of 15 l min^{-1} and a sampling duration of 30 min to derive the "adjusted LOD_{conc}" of our

instrument. Hereafter, we simply refer to "adjusted LOD_{conc}" as "LOD" unless otherwise stated.

Consistent with the results obtained from wavelength selection (Section 3.1) and despite their impressive adjusted R^2 and normalized RMSE, Cd and Hg have the highest (i.e., worst) LOD among the 13 elements (Fig. 4). For the other elements, the LOD based on univariate calibration is in the range of 0.06–0.19 μg m^{-3}, with the lowest LOD for Be and the highest one for Zn. Among the three multivariate calibration models, LASSO has the best LODs ranging from 0.03 to 0.11 μg m^{-3}. By comparing the univariate and LASSO models, relatively large differences are found for Co and Ni, where the LODs based on LASSO are about 4 times better (lower) than those using the univariate method. Overall, LASSO outperforms the other approaches in terms of LODs, indicating better suitability for determining elements with low concentration.

The LODs derived by the LASSO approach using the TARTA are then compared to the LODs based on other analytical instruments, such as the aerosol spark emission spectroscopy (ASES) instrument tested in Zheng et al. (2018), inductively coupled plasma mass spectrometry (ICP-MS), and the XRF instrument (Xact 625, Cooper Environmental Inc.). The spark discharge process of ASES is similar to TARTA when detecting particulate matter, but its sampling system tends to be more complicated because ASES requires a corona aerosol micro-concentrator to charge and direct particles onto the ground electrode (Diwakar & Kulkarni, 2012; Zheng, Kulkarni, Birch, Deye, & Dionysiou, 2016). Though widely used for elemental determination, both ICP-MS and XRF are expensive approaches that require skilled operations. Furthermore, these are laboratory, off-line techniques making them unsuitable for quick and real-time measurements (Evans et al., 2020). Although Xact 625 has achieved relatively high temporal resolution (15–240 min) by an automated moveable filter tape system, its high cost and complexity may prevent its use at multiple observation sites (Fujita & Campbell, 2013; Furger et al., 2017; Ryder et al., 2020). Besides the mentioned instruments, many other techniques can be used to measure atmospheric metal concentrations, such as X-ray fluorescence analyzer from Horiba Inc and ICP-OES from SPECTRO Analytical Instruments Inc. However, a detailed inter-comparison of these techniques is beyond the scope of this work.

For most of the metals presented in Table 2, TARTA has LODs similar to ASES and ICP-MS, but more than 10 times greater LODs than Xact 625. It is worth noting that the two SIBS instruments (TARTA and ASES, both sampling at a 30-min interval) yield very consistent LODs for Cr, Cu, Fe, Mn, and Ni, although their particle loading systems are different. For Fe and K, the LODs derived by ICP-MS and Xact 625 are much greater than that for the other elements; however this discrepancy is not observed for the two SIBS instruments. Although TARTA is not as sensitive as Xact 625, the two instruments represent a trade-off between cost and performance – the TARTA can be built for only about $5000 (using the Ocean Optics spectrometer employed in this work) or $3000 (using lower-cost spectrometers, such as LR1 spectrometer from ASEQ instruments Inc.), whereas the Xact costs about $150,000. Consequently, the combination of LASSO and the instrument developed in our study is promising for cost-effectively quantifying mass concentration of metal particles.

3.4. Prediction of unknown samples

The ultimate goal of this study is to build a more accurate and robust calibration model for SIBS quantitative analysis of multielemental emissions, so we further validate the LASSO models (the best approach as presented above) by exploring its predictions for samples not used during the training phase. Different from the single-component solutions used before, the validation datasets are mixtures of different elemental solutions.

The first type of validation datasets consists of 10 elements (i.e., Cr, Mn, Cu, Ni, Fe, Zn, Co, Hg, Cd, and Pb) at two concentration levels (1 and 5 μg ml^{-1}). K, Be, and Al which are not added to the solution serve as the control group. The estimated C_{tot} of each element is plotted versus sampling duration in Fig. 5 and versus "true" C_{tot} in Figure S6. According to the definition in Eq. (3), the slope of the line fitting the data in Fig. 5 represents the predicted elemental air concentration. Except for Hg, Cd, Pb, and the metals in the control group, the change of sampling duration and elemental solution concentration can be well estimated by the LASSO models ($R^2 > 0.9$). Comparing the slopes of the fitting lines, the predicted air concentrations of these metals are 6.01 ± 1.08 μg m^{-3} (5 μg ml^{-1} solution) and 1.67 ± 0.10 μg m^{-3} (1 μg ml^{-1} solution). For Hg and Cd, the predicted mass concentrations are lower than that for the other metals, and the R^2 values are reduced for the experiments using 1 μg ml^{-1} solutions. Interestingly, although Pb shows strong correlations with $R^2 > 0.95$, the predicted mass concentration is close to or lower than the calculated LODs (e.g., 2.8 μg m^{-3} (2-min sampling) and 0.28 μg m^{-3} (15-min sampling)). For K, Be, and Al (control group), no significant difference of mass concentration is observed when varying sampling duration and solution concentration, which indicates that the LASSO models are suitable to identify the presence of elements in the sample.

Another type of validation dataset mimics the elemental composition of particulate matter commonly found in North America, where the percentage of each compound in the mixture is taken from literature. Comparing the elements tested in our study to those reported in Mamun, Cheng, Zhang, Dabek-Zlotorzynska, and Charland (2019), Zn, Cu, K, Al belong to the predominant elements in both PM2.5 and PM10 (greater than 10 ng m^{-3}), whereas Co, Cd, Be are the least abundant (less than 1 ng m^{-3}). We therefore designed a test solution with concentrations of 5 μg ml^{-1} for Fe, Zn, K, and Al, 1 μg ml^{-1} for Mn, Ni, Cu, Pb, Cr, and Hg, and 0.5 μg ml^{-1} for Co, Cd, and Be. Similar to Fig. 5, the relationship between C_{tot} and sampling duration for this validation dataset can be found in Figure S7. The regression results (slope and R^2) of the fitting lines are summarized in Table 3. The slope results (i.e., elemental concentration) suggest that the LASSO approach is able to quantify most of the elements from solutions with different concentrations (6.25 ± 0.61 μg m^{-3} (5 μg ml^{-1} solution), 1.97 ± 0.71 μg m^{-3} (1 μg ml^{-1} solution), and 0.87 ± 0.31 μg m^{-3} (0.5 μg ml^{-1} solution)). Furthermore, the estimates are reasonably robust because the R^2 results are fairly strong. For the elements that have the same solution concentrations in the two types of dataset, we also conducted t-tests to examine if the predicted mass concentrations are statistically different (Table 3). All t-values for 95% confidence interval are not significant (P value < 0.05), indicating no significant differences.

3.5. Measurement uncertainty

Clearly, the analytical method presented in this work can enhance the quantification of elemental mass concentrations using TARTA in terms of improved LOD and reduced matrix effect, but understanding and accounting for measurement uncertainty is also important. First of all, reproducibility of plasma is evaluated by calculating the coefficient of variation (CV) of W signals (429.77 nm, from electrode) and O signals (777.76 nm, from ambient environment) for repeated spark generations. Based on the results of 100 consecutive sparks, the CV was found to be 10% (W) and 19% (O) when using the data of the original spectra, but reduced to 6% (W) and 12% (O) after normalization. These variations are of the same magnitude as those reported in a previous study using SIBS to measure aerosol concentration (Diwakar & Kulkarni, 2012). Second, another source of measurement uncertainty is associated with the variation of collection efficiency. According to Zheng et al. (2017), the collection efficiency of SIBS is governed by particle size, air flow rate, and characteristics of electrical components (such as interelectrode distance, electrode diameter, and corona current). Their study found that the collection efficiency remains relatively stable for particle sizes below 1 μm, but greater flow rate can increase uncertainty of analyte signals because there may be increased bounce of particles at high flow rate. Since our experimental setup has been optimized as described in Li et al. (2021) and we simply tested particles with a mean size of 0.55 μm, it is probable that the variation of collection efficiency has been sufficiently reduced. However, further studies are necessary to determine the measurement efficiency of TARTA for large particles. Lastly, uncertainty can propagate from the calibration procedure. Based on an uncertainty of 18% in APS-derived particle mass concentration (Buonanno, Dell'Isola, Stabile, & Viola, 2009) and an uncertainty of 6.8% in the training process of the LASSO models (normalized RMSE in Fig. 3), we estimate a 19% uncertainty of our calibration (quadrature method).

4. Conclusions

Different multivariate calibration models (LASSO, PCR, PLS, and SVR) were constructed to determine mass concentration of metal particles nebulized from aqueous solutions. To this end, the raw spectra derived by an inexpensive SIBS system were preprocessed by baseline correction and normalization using an internal standard (a strong emission line from the electrode) to minimize matrix effects. By using an automatic peak detection algorithm, representative peaks of each metal were identified and used as input to the machine learning models. After model development, we found that the most influential wavelengths identified by the models agree well with one or multiple strong elemental lines from the NIST atomic spectral database. Our results suggest that the regression coefficients of the machine learning models can be used to determine meaningful emission lines related to the sample.

Comparing to univariate calibration models, machine learning models have better performance in terms of adjusted R^2 and normalized RMSE. Among the models, LASSO has superior performance, with adjusted R^2 of 0.80–0.97 and normalized RMSE of 0.02–0.13. The relatively poor performance of SVR implies that non-linear approaches may not be suitable for analyzing the samples studied in this work. However, it remains uncertain how these models perform for samples with more complicated chemical matrix effects.

Based on the LASSO models, we calculated the LODs for different elements and compared the result to that of other analytical techniques. The TARTA has LODs ranged from 0.04 μg m^{-3} (Mn) to 0.17 μg m^{-3} (Hg) at a sampling duration of 30 min and a flow rate of 15 l min^{-1}, which are very similar to the LODs reported for ASES and ICP-MS. Although the LODs of our instrument are greater than those of the Xact 625 by an order of magnitude, the cost of the Xact is more than an order of magnitude great than our instrument. For the metals that are difficult to quantify because of relatively poor LODs and calibration results (i.e., Cd, Hg, and Pb), the TARTA can still be used to detect their presence in near-real time at the observational site. After detection, the other analytical techniques with lower LODs may be used off-line for elemental analysis.

Lastly, when applied to independent validation datasets (mixtures of 10 or 13 types of metals with different solution concentrations), the mass concentration predicted by the LASSO models show good agreement with known concentrations of each analyte. Overall, a combination of the TARTA and the proposed LASSO approach is very promising for identifying and quantifying air contaminants in various environments.

Supplementary Material

Refer to Web version on PubMed Central for supplementary material.

Funding

This research has been funded by the California Air Resources Board, contract 17RD022.

References

Aldabe J, Santamaría C, Elustondo D, Lasheras E, & Santamaría JM (2013). Application of microwave digestion and ICP-MS to simultaneous analysis of major and trace elements in aerosol samples collected on quartz filters. Analytical Methods, 5(2), 554–559. 10.1039/C2AY25724F

Allegrini F, & Olivieri AC (2014). IUPAC-consistent approach to the limit of detection in partial least-squares calibration. Analytical Chemistry, 86(15), 7858–7866. 10.1021/ac501786u [PubMed: 25008998]

Braga JWB, Trevizan LC, Nunes LC, Rufini IA, Santos D, & Krug FJ (2010). Comparison of univariate and multivariate calibration for the determination of micronutrients in pellets of plant materials by laser induced breakdown spectrometry. Spectrochimica Acta Part B: Atomic Spectroscopy, 65(1), 66–74. 10.1016/j.sab.2009.11.007

Brereton RG (2000). Introduction to multivariate calibration in analytical chemistry. Analyst, 125(11), 2125–2154. 10.1039/b003805i

Bricklemyer RS, Brown DJ, Turk PJ, & Clegg SM (2013). Improved intact soil-core carbon determination applying regression shrinkage and variable selection techniques to complete spectrum laser-induced breakdown spectroscopy (LIBS). Applied Spectroscopy, 67(10), 1185–1199. 10.1366/12-06983 [PubMed: 24067576]

Bro R (2003). Multivariate calibration. Analytica Chimica Acta, 500(1–2), 185–194. 10.1016/S0003-2670(03)00681-0

Chong I-G, & Jun C-H (2005). Performance of some variable selection methods when multicollinearity is present. Chemometrics and Intelligent Laboratory Systems, 78(1–2), 103–112. 10.1016/j.chemolab.2004.12.011

Cortes C, & Vapnik V (1995). Support-vector networks. Machine Learning, 20(3), 273–297.

Davari SA, & Wexler AS (2020). Quantification of toxic metals using machine learning techniques and spark emission spectroscopy. Atmospheric Measurement Techniques, 13(10), 5369–5377. 10.5194/amt-13-5369-2020 [PubMed: 38596355]

Diwakar PK, & Kulkarni P (2012). Measurement of elemental concentration of aerosols using spark emission spectroscopy. Journal of Analytical Atomic Spectrometry, 27(7), 1101. 10.1039/c2ja30025g [PubMed: 26491209]

Drucker H, Burges CJC, Kaufman L, Smola AJ, & Vapnik V (1997). Support vector regression machines. Advances in Neural Information Processing Systems, 155–161.

Durhan EJ, Norberg-King TJ, & Burkhard LP (1993). Methods for aquatic toxicity identification evaluations: Phase II toxicity identification procedures for samples exhibiting acute and chronic toxicity. U.S. Environmental Protection Agency, Office of Research and Development.

EPA. (2017). Initial list of hazardous air pollutants with modifications. Retrieved from US Environmental Protection Agency website. https://www.epa.gov/haps/initial-list-hazardous-air-pollutants-modifications.

Evans EH, Pisonero J, Smith CMM, & Taylor RN (2020). Atomic spectrometry update: Review of advances in atomic spectrometry and related techniques. Journal of Analytical Atomic Spectrometry, 35(5), 830–851. 10.1039/D0JA90015J

Fu X, Duan F-J, Huang T-T, Ma L, Jiang J-J, & Li Y-C (2017). A fast variable selection method for quantitative analysis of soils using laser-induced breakdown spectroscopy. Journal of Analytical Atomic Spectrometry, 32(6), 1166–1176. 10.1039/C7JA00114B

Fu H, Jia J, Wang H, Ni Z, & Dong F (2018). Calibration methods of laser-induced breakdown spectroscopy. In Calibration and validation of analytical methods - a sampling of current approaches. 10.5772/intechopen.72888

Fujita EM, & Campbell DE (2013). Review of current air monitoring capabilities near refineries in the San Francisco Bay area. Desert Research Institute.

Furger M, Minguillón MC, Yadav V, Slowik JG, Hüglin C, Fröhlich R, et al. (2017). Elemental composition of ambient aerosols measured with high temporal resolution using an online XRF spectrometer. Atmospheric Measurement Techniques, 10(6), 2061–2076. 10.5194/amt-10-2061-2017

Geladi P, & Kowalski BR (1986). Partial least-squares regression: A tutorial. Analytica Chimica Acta, 185, 1–17. 10.1016/0003-2670(86)80028-9

Haaland DM, & Thomas EV (1988). Partial least-squares methods for spectral analyses. 2. Application to simulated and glass spectral data. Analytical Chemistry, 60(11), 1202–1208. 10.1021/ac00162a021

Hahn DW, & Omenetto N (2010). Laser-induced breakdown spectroscopy (LIBS), Part I: Review of basic diagnostics and plasma—particle interactions: Still-challenging issues within the analytical plasma community. Applied Spectroscopy, 64(12), 335A–336A. 10.1366/000370210793561691 [PubMed: 21144145]

Hahn DW, & Omenetto N (2012). Laser-induced breakdown spectroscopy (LIBS), Part II: Review of instrumental and methodological approaches to material analysis and applications to different fields. Applied Spectroscopy, 66(4), 347–419. 10.1366/11-06574 [PubMed: 22449322]

Hunter AJR, Davis SJ, Piper LG, Holtzclaw KW, & Fraser ME (2000). Spark-induced breakdown spectroscopy: A new technique for monitoring heavy metals. Applied Spectroscopy, 54(4), 575–582. 10.1366/0003702001949753

Hunter AJR, Morency JR, Senior CL, Davis SJ, & Fraser ME (2000). Continuous emissions monitoring using spark-induced breakdown spectroscopy. Journal of the Air & Waste Management Association, 50(1), 111–117. 10.1080/10473289.2000.10463982 [PubMed: 10680371]

Hunter AJR, Wainner RT, Piper LG, & Davis SJ (2003). Rapid field screening of soils for heavy metals with spark-induced breakdown spectroscopy. Applied Optics, 42(12), 2102. 10.1364/AO.42.002102 [PubMed: 12716151]

Ismail MA, Imam H, Elhassan A, Youniss WT, & Harith MA (2004). LIBS limit of detection and plasma parameters of some elements in two different metallic matrices. Journal of Analytical Atomic Spectrometry, 19(4), 489. 10.1039/b315588a

IUPAC. (2019). The IUPAC compendium of chemical terminology. Gold V, Ed 10.1351/goldbook.

Jolliffe IT (1982). A note on the use of principal components in regression. Applied Statistics, 31(3), 300. 10.2307/2348005

Jolliffe IT (1986). Principal component analysis and factor Analysis. In Principal component analysis (pp. 115–128). 10.1007/978-1-4757-1904-8_7

Jung J, Yang J-H, & Yoh JJ (2020). An optimal configuration for spark-induced breakdown spectroscopy of bulk minerals aimed at planetary analysis. Journal of Analytical Atomic Spectrometry, 35(6), 1103–1114. 10.1039/D0JA00057D

Khan A, Munir MT, Yu W, & Young B (2020). Wavelength selection for rapid identification of different particle size fractions of milk powder using hyperspectral imaging. Sensors, 20(16), 4645. 10.3390/s20164645 [PubMed: 32824764]

Koelmel JP, Cochran JA, Ulmer CZ, Levy AJ, Patterson RE, Olsen BC, et al. (2019). Software tool for internal standard based normalization of lipids, and effect of data-processing strategies on resulting values. BMC Bioinformatics, 20(1), 217. 10.1186/s12859-019-2803-8 [PubMed: 31035918]

Lepore KH, Fassett CI, Breves EA, Byrne S, Giguere S, Boucher T, et al. (2017). Matrix effects in quantitative analysis of laser-induced breakdown spectroscopy (LIBS) of rock powders doped with Cr, Mn, Ni, Zn, and Co. Applied Spectroscopy, 71(4), 600–626. 10.1177/0003702816685095 [PubMed: 28374610]

Li H, & May AA (2020). An exploratory approach using regression and machine learning in the analysis of mass absorption cross section of black carbon aerosols: Model development and evaluation. Atmosphere, 11(11), 1185. 10.3390/atmos11111185

Li H, Mazzei L, Wallis CD, Davari SA, & Wexler AS (2021). The performance of an inexpensive spark-induced breakdown spectroscopy instrument for near real-time analysis of toxic metal particles. Atmospheric Environment, 118666. 10.1016/j.atmosenv.2021.118666

Mamun A. Al, Cheng I, Zhang L, Dabek-Zlotorzynska E, & Charland J-P (2019). Overview of size distribution, concentration, and dry deposition of airborne particulate elements measured worldwide. Environmental Reviews, 1–12. 10.1139/er-2019-0035

Melkumova LE, & Shatskikh SY (2017). Comparing Ridge and LASSO estimators for data analysis. Procedia Engineering, 201, 746–755. 10.1016/j.proeng.2017.09.615

Miziolek AW, Palleschi V, & Schechter I (Eds.). (2006). Laser-induced breakdown spectroscopy (LIBS). 10.1017/CBO9780511541261

Næs T, & Martens H (1984). Multivariate calibration. II. Chemometric methods. TRAC Trends in Analytical Chemistry, 3(10), 266–271. 10.1016/0165-9936(84)80044-8

Nicolini O (2020). LIBS multivariate analysis with machine learning.

Olivieri AC (2018). Introduction to multivariate calibration. 10.1007/978-3-319-97097-4.

Ralchenko Y, Jou FC, Kelleher DE, Kramida A, Musgrove A, Reader J, et al. (2006). Nist atomic spectra database (version 3.1. 0).

Ryder OS, DeWinter JL, Brown SG, Hoffman K, Frey B, & Mirzakhalili A (2020). Assessment of particulate toxic metals at an Environmental Justice community. Atmospheric Environment X, 6, 100070. 10.1016/j.aeaoa.2020.100070

Schulze HG, Foist RB, Okuda K, Ivanov A, & Turner RFB (2012). A small-window moving average-based fully automated baseline estimation method for Raman spectra. Applied Spectroscopy, 66(7), 757–764. 10.1366/11-06550 [PubMed: 22710274]

Shao X, Bian X, Liu J, Zhang M, & Cai W (2010). Multivariate calibration methods in near infrared spectroscopic analysis. Analytical Methods, 2(11), 1662. 10.1039/c0ay00421a

Takahashi T, & Thornton B (2017). Quantitative methods for compensation of matrix effects and self-absorption in Laser Induced Breakdown Spectroscopy signals of solids. Spectrochimica Acta Part B: Atomic Spectroscopy, 138, 31–42. 10.1016/j.sab.2017.09.010

Tibshirani R (1996). Regression shrinkage and selection via the lasso. Journal of the Royal Statistical Society: Series B, 58(1), 267–288.

Tognoni E, & Cristoforetti G (2016). [INVITED] signal and noise in laser induced breakdown spectroscopy: An introductory review. Optics & Laser Technology, 79, 164–172. 10.1016/j.optlastec.2015.12.010

Wang T, He M, Shen T, Liu F, He Y, Liu X, et al. (2018). Multi-element analysis of heavy metal content in soils using laser-induced breakdown spectroscopy: A case study in eastern China. Spectrochimica Acta Part B: Atomic Spectroscopy, 149, 300–312. 10.1016/j.sab.2018.09.008

Wold S, Sjöström M, & Eriksson L (2001). PLS-regression: A basic tool of chemometrics. Chemometrics and Intelligent Laboratory Systems, 58(2), 109–130. 10.1016/S0169-7439(01)00155-1

Yang J-H, Jung J, Ryu J-H, & Yoh JJ (2020). Real-time monitoring of toxic components from fine dust air pollutant samples by utilizing spark-induced plasma spectroscopy. Chemosphere, 257, 127237. 10.1016/j.chemosphere.2020.127237 [PubMed: 32512334]

Yao S, Zhang L, Xu J, Yu Z, & Lu Z (2017). Data processing method for the measurement of unburned carbon in fly ash by PF-SIBS. Energy & Fuels, 31(11), 12093–12099. 10.1021/acs.energyfuels.7b02692

Yaroshchyk P, Death DL, & Spencer SJ (2012). Comparison of principal components regression, partial least squares regression, multi-block partial least squares regression, and serial partial least squares regression algorithms for the analysis of Fe in iron ore using LIBS. Journal of Analytical Atomic Spectrometry, 27(1), 92–98. 10.1039/C1JA10164A

Yin P, & Fan X (2001). Estimating R 2 shrinkage in multiple regression: A comparison of different analytical methods. The Journal of Experimental Education, 69(2), 203–224. 10.1080/00220970109600656

Yoder N (2021). Peakfinder(x0, sel, thresh, extrema, include endpoints, interpolate). MATLAB Central File Exchange. Retrieved from https://www.mathworks.com/matlabcentral/fileexchange/25500-peakfinder-x0-sel-thresh-extrema-includeendpoints-interpolate.

Zaytsev SM, Krylov IN, Popov AM, Zorov NB, & Labutin TA (2018). Accuracy enhancement of a multivariate calibration for lead determination in soils by laser induced breakdown spectroscopy. Spectrochimica Acta Part B: Atomic Spectroscopy, 140, 65–72. 10.1016/j.sab.2017.12.005

Zheng L, & Kulkarni P (2017). Rapid elemental analysis of aerosols using atmospheric glow discharge optical emission spectroscopy. Analytical Chemistry, 89(12), 6551–6558. 10.1021/acs.analchem.7b00691 [PubMed: 28513144]

Zheng L, Kulkarni P, Birch ME, Deye G, & Dionysiou DD (2016). Near real-time measurement of carbonaceous aerosol using microplasma spectroscopy: Application to measurement of carbon nanomaterials. Aerosol Science and Technology, 50(11), 1155–1166. 10.1080/02786826.2016.1224804 [PubMed: 28638174]

Zheng L, Kulkarni P, & Dionysiou DD (2018). Calibration approaches for the measurement of aerosol multielemental concentration using spark emission spectroscopy. Journal of Analytical Atomic Spectrometry, 33(3), 404–412. 10.1039/C7JA00252A [PubMed: 35673324]

Zheng L, Kulkarni P, Zavvos K, Liang H, Birch ME, & Dionysiou DD (2017). Characterization of an aerosol microconcentrator for analysis using microscale optical spectroscopies. Journal of Aerosol Science, 104, 66–78. 10.1016/j.jaerosci.2016.11.007 [PubMed: 28626243]

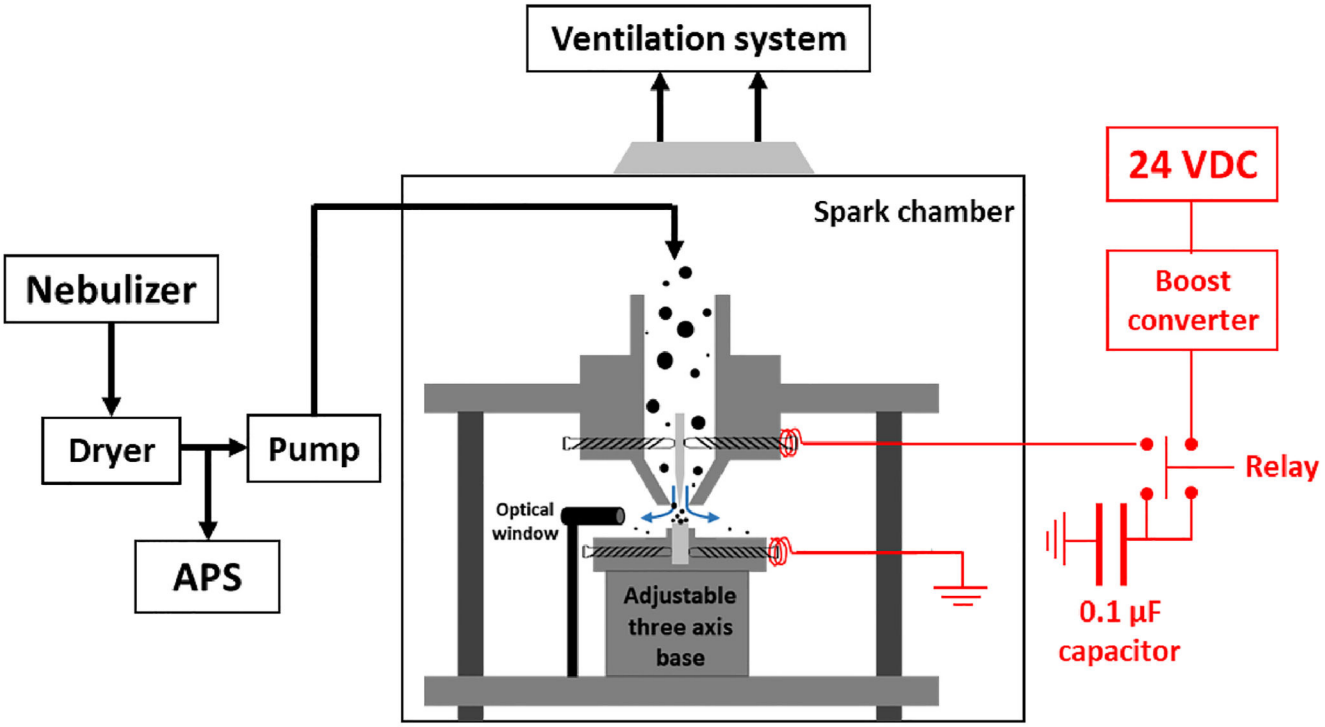

Fig. 1.
Schematic of the experimental setup.

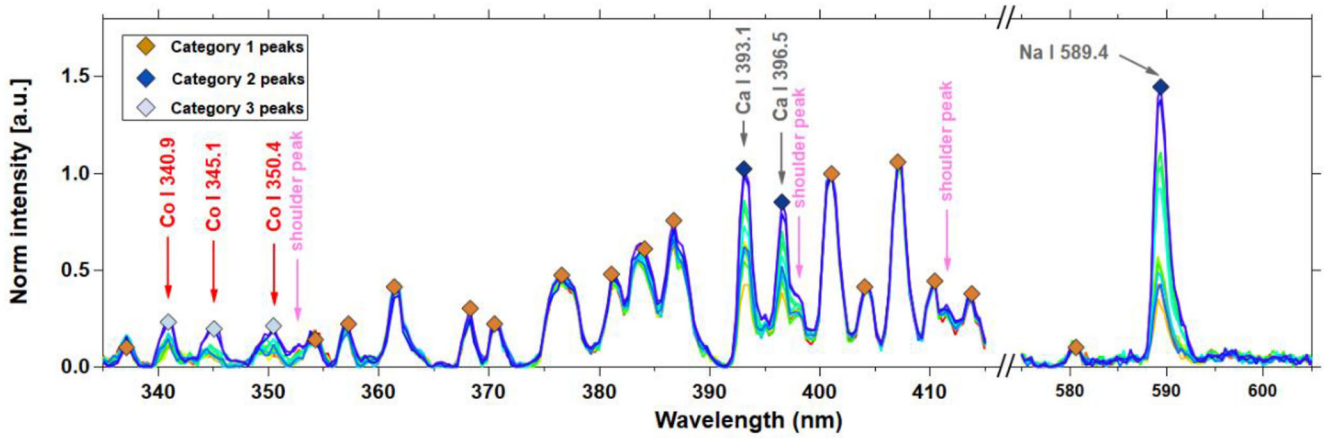

Fig. 2.

SIBS results for the analysis of Co. For better illustration, we only present the results from 330 to 605 nm. Each curve represents the normalized spectra obtained from an experiment. The different categories of spectral peaks are represented by diamond symbols with different colors. Note that the x-axis is broken from 420 to 570 nm.

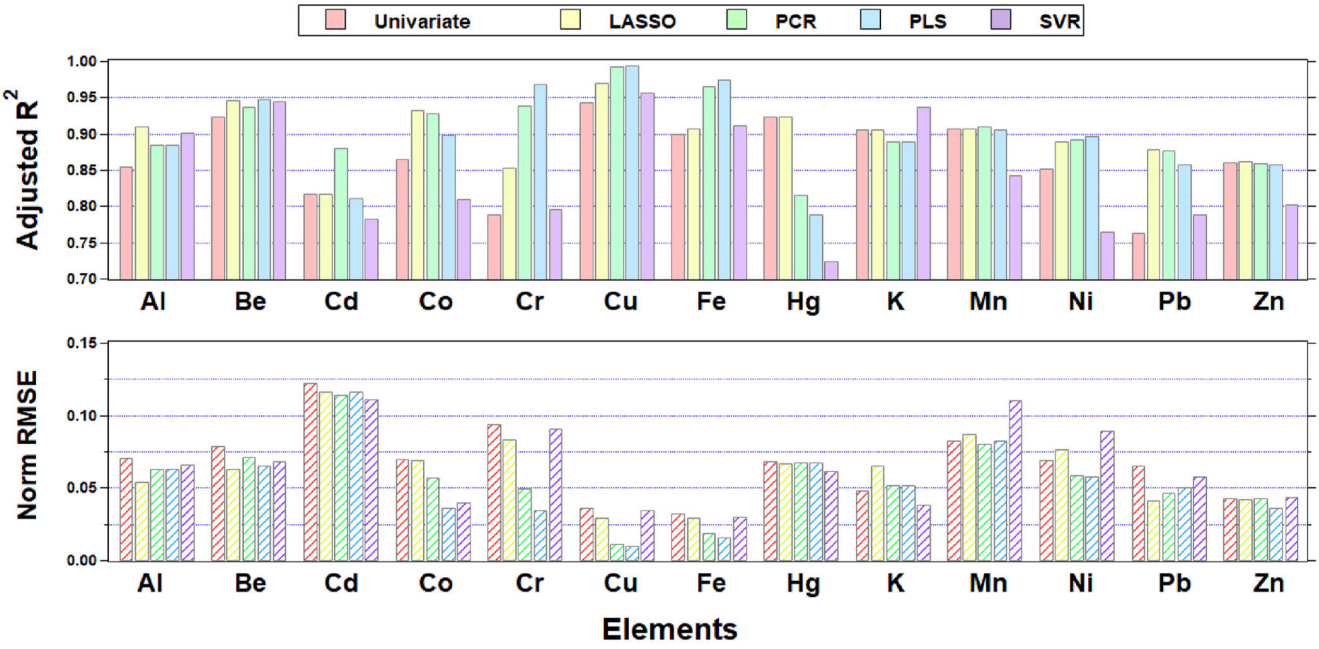

Fig. 3.

Adjusted R^2 and RMSE results derived by different calibration models for the training dataset of each metal.

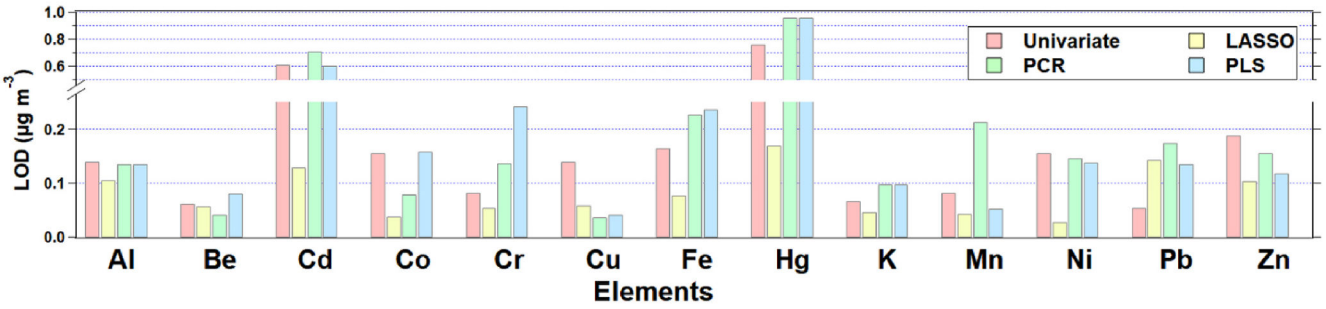

Fig. 4.

Comparison of adjusted LOD_{conc} estimated by different approaches used in this work. We exclude SVR results, because SVR behaves relatively poorly during model development and is not able to derive LODs using Eqs. (4) and (5). Note that the y-axis is broken from 0.25 to 0.5 μg m^{-3}.

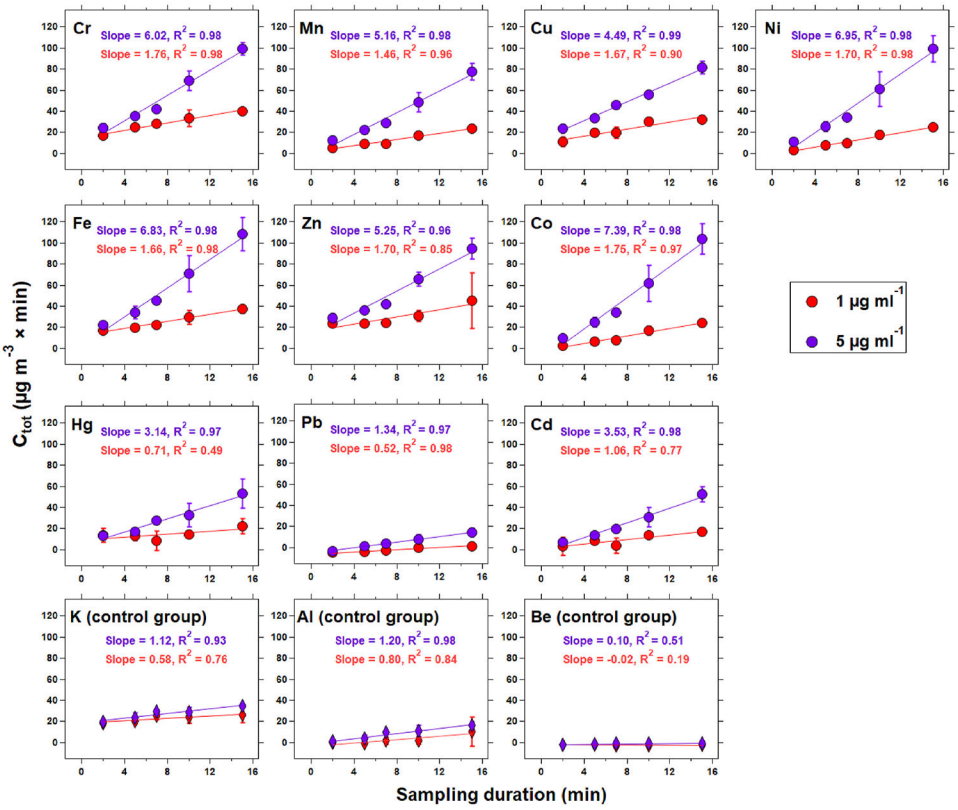

Fig. 5.

Estimated C_{tot} (the integration of mass concentration over the sampling period) when applying LASSO models to independent validation datasets.

Table 1

Summary of preprocessed peaks and elemental emission lines selected by different calibration models.

Element	Number of peaks[a]	Number of peaks after exclusion[b]	Strong emission lines (nm) from NIST database[c]	Wavelengths (nm) selected by LASSO[d]	Important wavelengths (nm) derived by PCR[e]	Important wavelengths (nm) derived by PLS[e]	Important wavelengths (nm) derived by SVR[e]
Al	53	1	307.8, **309.1**	309.9, 308.8, 309.1, 308.4	308.8, 309.1, 308.4	309.1, 308.8, 308.4	310.3, 308.4, 309.5
Be	46	1	**313.0**	311.8, 312.6	313.0, 312.6, 313.4	313.0, 312.6, 313.4	312.2, 313.4, 314.1
Cd	75	15	**508.3**	508.3	419.7, 452.4, 559.7	537.9, 412.3, 559.7	537.9, 518.5, 340.9
Co	69	3	340.9, **345.1**, 350.4, 356.9	345.1, 345.5, 344.3, 344.7	345.1, 344.7, 356.9	345.1, 344.7, 345.5	341.7, 358.0, 344.0
Cr	38	4	357.8, 425.4, 427.2, 442.4, **520.3**	426.1	519.9, 442.0, 356.5	356.5, 442.4, 442.8	358.4, 443.5, 443.1
Cu	71	3	**324.5**, 327.2	327.2, 327.5	324.5, 324.8, 327.2	324.9, 327.2, 324.5	325.6, 328.3, 325.2
Fe	58	2	344.0, **373.6**, 385.9, 438.3	373.6, 343.2, 373.9	373.9, 373.6, 374.3	373.6, 373.9, 374.7	374.3, 373.2, 344.7
Hg	60	9	**546.1**	546.1	337.9, 489.8, 518.5	518.5, 546.1, 337.9	474.4, 329.8, 412.3
K	71	2	**766.8**, 770.0	766.8	770.3, 766.8, 770.0	767.1, 766.4, 769.0	769.0, 770.3, 765.8
Mn	41	1	**403.3**	403.3, 403.7, 404.4	403.3, 402.9, 403.7	402.9, 403.7, 403.3	404.4, 402.2, 404
Ni	65	3	341.4, **352.3**, 356.9	352.3, 351.6, 352.0	352.0, 351.6, 352.3	352.3, 352.0, 351.6	353.1, 340.5, 340.1
Pb	55	3	**405.9**	404.8, 407.0, 405.5, 406.7	405.5, 404.8, 405.9	407.0, 405.9, 405.5	407.0, 406.6, 405.1
Zn	58	2	334.0, 472.2, **481.0**	481.0, 481.4	479.9, 333.7, 481.4	479.9, 334.8, 480.3	335.2, 479.9, 333.7

[a] The peaks were automatically determined using a peak detection algorithm (Yoder, 2021).

[b] After removing the redundant wavelengths, the surrounding 6 wavelengths (3 before and 3 after) of each peak were added to develop machine learning models (See section 2.2.2 and Table S1 for more details).

[c] The wavelengths in bold were used to construct univariate calibration models.

[d] The selected wavelengths are ranked from most to least important according to variable importance of projection (VIP) scores.

[e] PCR, PLS, and SVM used all input wavelengths to develop calibration models, but we only present the top three important wavelengths (based on VIP scores) in the table.

Table 2

Comparison of LODs (μg m^{-3}) generated by the TARTA and other analytical methods. All results are estimated at a 30 min sampling duration.

Element	TARTA[a]	ASES[b] (Zheng et al., 2018)	ICP-MS (Aldabe et al., 2013 ; Durhan et al., 1993)	Xact 625 (Ryder et al., 2020)
Al	0.11	-	0.03	0.012
Be	0.06	-	0.05	-
Cd	0.13	0.02	0.05	0.001
Co	0.08	-	0.02	-
Cr	0.05	0.05	0.04	0.003
Cu	0.06	0.04	0.02	0.001
Fe	0.08	0.08	2.00	0.031
Hg	0.17	-	-	<0.001
K	0.05	-	2.50	0.048
Mn	0.04	0.04	0.05	0.001
Ni	0.09	0.07	0.10	0.003
Pb	0.14	0.08	0.04	0.006
Zn	0.10	0.06	0.10	0.014

[a] The results are calculated using the LASSO approach.

[b] The ASES sampled aerosols in a corona aerosol micro-concentrator at a flow rate of 2 l min^{-1}.

Table 3

LASSO results of the second type of validation dataset.

Solution concentration (μg ml^{-1})	Element	Slope (i.e., elemental concentration, μg m^{-3})[a]	R^2	Reference elemental concentration (μg m^{-3})[b]	T test statistic[c]
5	Zn	6.20	0.98	5.25	−0.09
	Fe	6.23	0.99	6.83	−0.15
	K	5.55	0.97	-	-
	Al	7.05	0.97	-	-
1	Cr	2.58	0.95	1.76	−0.63
	Cu	2.51	0.98	1.67	−1.16
	Mn	2.31	0.99	1.46	−1.04
	Ni	2.29	0.99	1.70	−0.62
	Pb	1.06	0.99	0.52	−0.93
	Hg	1.08	0.99	0.71	−1.81
0.5	Co	0.66	0.99	-	-
	Cd	1.22	0.99	-	-
	Be	0.72	0.69	-	-

[a] The slope is based on the regression results in Figure S7.

[b] Reference elemental concentrations are the slopes of the fitting lines in Fig. 5. Note that the results of K, Al, and Be (control group), and 0.5 μg ml^{-1} Co and Cd are not available in the first validation dataset.

[c] T-test compares the mean of the two columns of elemental concentration in relation to the variation in the data. The closer T-value is to 0, the better the agreement is.